

Finite-volume time-domain (FVTD) modelling of a broadband double-ridged horn antenna

Dirk Baumann^{*,†}, Christophe Fumeaux, Pascal Leuchtman
and Rüdiger Vahldieck

*Laboratory for Electromagnetic Fields and Microwave Electronics (IFH), Swiss Federal Institute of Technology (ETH)
Zurich, Zurich 8092, Switzerland*

SUMMARY

This paper demonstrates the suitability of the finite-volume time-domain (FVTD) method to analyse electromagnetic 'real-world' problems. As a challenging example, a 1–18 GHz broadband double-ridged horn antenna is chosen. The horn antenna consists of non-orthogonal and curved parts and a small coaxial feeding that is modelled in detail. The simulation results of the far-field patterns, the return loss and the gain are successfully compared to measurements. They show that the FVTD method—using an inhomogeneous tetrahedral mesh—is very well suited for simulating complex structures. Copyright © 2004 John Wiley & Sons, Ltd.

KEY WORDS: FVTD; double-ridged horn antenna

1. INTRODUCTION

The finite-volume time-domain (FVTD) technique solves partial differential equations of hyperbolic nature in conservative form. It was applied very successfully in computational fluid dynamics and since the end of the 1980s it is used for the numerical solution of Maxwell's equations [1, 2]. Since the FVTD method is performed in unstructured conformal meshes it is very well suited for modelling structures including curved or oblique surfaces and fine structural details in close proximity to large assemblies. These problems represent a big challenge in computational electromagnetics. Exploiting the geometrical flexibility of inhomogeneous meshes the FVTD method constitutes a powerful alternative to the classical FDTD Yee scheme that uses stair-casing approximations and sub-gridding to model complex structures. Modifications of the original Yee algorithm for irregular meshes exist at the cost of an increased complexity. The FVTD method—in spite of the larger cost per cell—saves memory resources in comparison to the classical FDTD algorithm by reducing significantly the number of cells

*Correspondence to: D. Baumann, Laboratory for Electromagnetic Fields and Microwave Electronics (IFH), Swiss Federal Institute of Technology (ETH) Zurich, Zurich 8092, Switzerland.

†E-mail: dbaumann@ifh.ee.ethz.ch

Contract/grant sponsor: Swiss Defense Procurement Agency (Armasuisse)

necessary for accurate simulation of complex problems. The simulation of the broadband double-ridged horn antenna is a demanding task for numerical simulations due to the large dimensions with respect to the wavelength at the highest operational frequency, curved and non-orthogonal surfaces and a very small feed structure. The large bandwidth puts hard requirements on the mesh: keeping the amount of cells as low as possible while assuring spatial convergence over the total frequency range. Up to now only Bruns *et al.* [3] performed a complete broadband numerical analysis of that antenna including the coaxial feed, using the method of moments.

In this paper the principle steps for the FVTD method are presented first. Then the broadband double-ridged horn characteristics are described. Using the measurements presented in Reference [3], the ability of the FVTD method to accurately and efficiently handle such complex structures is demonstrated here.

2. THE FVTD SCHEME

In the FVTD method, the Maxwell's curl equations in conservative form [4] are integrated over an elementary polyhedral volume V_i using the divergence theorem

$$\begin{aligned} -\frac{\partial}{\partial t} \iiint_{V_i} \mathbf{B} dv &= \iint_{\partial V_i} \mathbf{n} \times \mathbf{E} da = \sum_{k=1}^{N_i} \mathbf{n}_k \times \iint_{F_k} \mathbf{E} da \\ \frac{\partial}{\partial t} \iiint_{V_i} \mathbf{D} dv &= \iint_{\partial V_i} \mathbf{n} \times \mathbf{H} da = \sum_{k=1}^{N_i} \mathbf{n}_k \times \iint_{F_k} \mathbf{H} da \end{aligned} \quad (1)$$

In these equations, ∂V_i represents the boundary of the elementary volume V_i that is composed of N_i planar faces. Each face has the area F_k ($k = 1, \dots, N_i$) and a normal unit vector \mathbf{n}_k that is pointing outwards of the corresponding cell. In the notation of the face area F_k and of the normal vector \mathbf{n}_k the index i of the corresponding volume is omitted for the sake of simplicity. To compute the exact equations (1) numerically, they are discretized as follows: The volume integrals on the left-hand side (LHS) are approximated by volume mean values of \mathbf{B} and \mathbf{D} in the considered volume V_i . On the right-hand side (RHS), the surface integrals are determined using the surface mean values of \mathbf{E} and \mathbf{H} over each face of the elementary cell. The discretized equations are then written as

$$\begin{aligned} -\frac{\partial}{\partial t} \langle \mathbf{B} \rangle_{V_i} &= \frac{1}{V_i} \sum_{k=1}^{N_i} (\mathbf{n}_k \times \langle \mathbf{E} \rangle_{F_k}) F_k \\ \frac{\partial}{\partial t} \langle \mathbf{D} \rangle_{V_i} &= \frac{1}{V_i} \sum_{k=1}^{N_i} (\mathbf{n}_k \times \langle \mathbf{H} \rangle_{F_k}) F_k \end{aligned} \quad (2)$$

where $\langle \cdot \rangle$ denotes a time-dependent spatial mean value. At this point the coupled equations (2) are still exact. The terms $\mathbf{n}_k \times \langle \mathbf{E} \rangle_{F_k}$ and $\mathbf{n}_k \times \langle \mathbf{H} \rangle_{F_k}$ on the RHS are interpreted as 'fluxes' through the cell faces. There are various implementations of the FVTD scheme, that differ in the numerical approximations of the coupled equations (2). In the FVTD algorithm presented here, tetrahedrons ($N_i = 4$) with a typical side length of $\lambda/10$ are used as elementary cells in a cell-centred FVTD scheme, where both the electric and the magnetic field components are defined at

the same location in the mesh (tetrahedral barycentre). Assuming that the electric permittivity ε and the magnetic permeability μ are linear, homogeneous, non-dispersive and isotropic in V_i , \mathbf{D} and \mathbf{B} can be related proportionally to \mathbf{E} and \mathbf{H}

$$\langle \mathbf{D} \rangle_{V_i} = \varepsilon \langle \mathbf{E} \rangle_{V_i} \quad \text{and} \quad \langle \mathbf{B} \rangle_{V_i} = \mu \langle \mathbf{H} \rangle_{V_i} \quad (3)$$

Inserting the material equations (3) into the discretized Maxwell's curl equations (2) permits to write approximate coupled equations for the time dependent $\langle \mathbf{E} \rangle$ and $\langle \mathbf{H} \rangle$ with their mean volume values located in the barycentre of the cells and their mean surface values located in the barycentre of the cell faces.

The 'fluxes' through the cell faces are computed from the field values in the face's adjacent cells and are closely related to the tangential fields on the faces. The commonly used FVTD schemes separate incoming and outgoing 'fluxes' through the surfaces. The separated 'fluxes' can be interpreted as contributions from plane waves propagating in positive $+\mathbf{n}_k$ (outgoing 'fluxes') and negative $-\mathbf{n}_k$ (incoming 'fluxes') direction through the cell face k taking into account the transmission coefficients [4].

For each face of a considered cell:

- outgoing 'fluxes' are estimated from barycentre values in the considered cell.
- incoming 'fluxes' are estimated from barycentre values in the neighbour cell.

In the algorithm presented here, second-order accuracy in space is achieved by using estimated gradients in the cell barycentres to compute the fields at the face centres according to the monotonic upwind scheme for conservation laws (MUSCL) [4].

The explicit FVTD update equations (including the 'flux' separation) can be written as

$$\begin{aligned} \langle \mathbf{H} \rangle_{V_i}^{n+1} &= \langle \mathbf{H} \rangle_{V_i}^n - \frac{\Delta t}{\mu V_i} \sum_{k=1}^4 \left(\mathbf{n}_k \times \overline{\langle \mathbf{E} \rangle_{F_k}^+} - \mathbf{n}_k \times \overline{\langle \mathbf{E} \rangle_{F_k}^-} \right) F_k \\ \langle \mathbf{E} \rangle_{V_i}^{n+1} &= \langle \mathbf{E} \rangle_{V_i}^n + \frac{\Delta t}{\varepsilon V_i} \sum_{k=1}^4 \left(\mathbf{n}_k \times \overline{\langle \mathbf{H} \rangle_{F_k}^+} - \mathbf{n}_k \times \overline{\langle \mathbf{H} \rangle_{F_k}^-} \right) F_k \end{aligned} \quad (4)$$

where the overline denotes a time mean value obtained by an integration over one time step Δt . On the RHS of (4) the 'fluxes' are separated into the outgoing (indicated with superscript $+$) and incoming part (superscript $-$). Second-order accuracy in time is attained applying the Lax–Wendroff predictor–corrector scheme [4]. Equation (4) then represents the time-corrector step, where the time-average values on the RHS were computed at the predictor step at a time half-step $(n + 1/2)$.

Independently of the time-marching scheme used, an FVTD time step can be separated basically into two stages as illustrated in Figure 1:

- (a) The field components on the faces of the cell are computed using field values at the barycentre of the considered cell and its direct neighbours.
- (b) The barycentre values are updated using 'fluxes' through the cell faces according to Equation (2) and following the chosen time-marching scheme.

In the following some relevant aspects of our FVTD implementation are described.

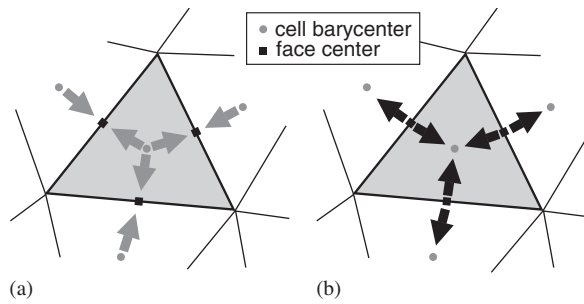


Figure 1. 2D illustration of the two stages of one FVTD iteration step: (a) Field values at face centres are computed from the values of the fields at adjacent barycentres; and (b) Barycentre values are updated using 'fluxes' through the faces.

2.1. Discretization

The commercial software Altair[®] HyperMesh[®] is used for drawing the model as well as generating the triangulated surfaces and the tetrahedral volume mesh [5]. HyperMesh uses the 'Advancing Front' algorithm to generate triangular surface meshes. In FVTD, a typical cell side length is $\lambda_{\min}/10$, where λ_{\min} corresponds to the wavelength at the highest occurring frequency in the simulation. Small geometrical features may demand significantly smaller discretizations. A characteristic and a main advantage of tetrahedral meshes are that two neighbouring cells always have one face in common. Hence, the transition from small to large cells or *vice versa* is always continuous and no spatial interpolation has to be performed. The non-uniformity of the mesh is crucial for the maximal time step Δt that assures stability. The cells with the worst volume to surface ratio determine the applicable time step according to

$$\Delta t \leq \frac{1}{c} \min_i \left(\frac{V_i}{\sum_{k=1}^{m_i} F_k} \right) \quad (5)$$

where c is the wave velocity in the medium. For an optimal time step and for good mesh quality non-uniform cells like flat and needle-like tetrahedrons should be avoided. The presence of non-uniform cells also results in a deterioration of the integral approximation in (2).

The only data that the commercial mesher has to transfer to our FVTD algorithm are the positions of the vertices of the surface triangles and the volume tetrahedrons. In our preprocessing the provided mesh data are transformed into interrelated cell, face and node lists that characterize mesh connectivity. Also, the material properties and the special cells and surfaces (as sources or boundaries) are stored and bookmarked.

2.2. Radiation boundary condition (RBC)

To limit the computational area a Silver-Müller RBC is implemented. This condition is perfectly suited for the FVTD algorithm since the incoming 'fluxes' into the computational area are simply set to zero

$$\begin{aligned} \mathbf{n}_k \times \langle \mathbf{E} \rangle_{F_k}^- &= 0 \\ \mathbf{n}_k \times \langle \mathbf{H} \rangle_{F_k}^- &= 0 \end{aligned} \quad (6)$$

To avoid reflection the outgoing waves have to impinge perpendicularly onto the boundary, since the Silver-Müller RBC only considers variations in the direction perpendicular to the boundary surface. For radiation problems (quasi-spherical waves), this requirement can be nearly satisfied by forming the outer boundary as a sphere. Hence, although the Silver-Müller condition is a first-order RBC, the geometrical flexibility of the outer boundary allows to enhance the accuracy much beyond that of a common first-order scheme. More sophisticated boundary conditions such as the Berenger's perfectly matched layers (PML) may be applicable as well, either by direct implementation into FVTD or in a hybrid FDTD-FVTD approach [6].

2.3. Excitation

To excite a structure (e.g. an antenna), energy has to be coupled into the system. In our FVTD algorithm two possibilities are introduced:

- point sources (hard/soft),
- constrained fields.

A point source introduces the electromagnetic energy by impressing the E - and/or the H -field either in a barycentre or through 'fluxes' at a triangular face-centre of a tetrahedron. Hard point sources impress the source field according to the excitation function. They may violate the continuity of the tangential fields and therefore cause reflections. In contrast, a soft source takes into consideration the field values of the former time step and thereby produces less reflections.

If the propagation mode of the feed is known *a priori* (as in a coaxial line) constrained fields can be used to excite the electromagnetic field in FVTD. The known field distribution is impressed on a transverse plane of the transmission line (that is called the source plane). The source fields are introduced as incoming 'fluxes' and thus are integrated naturally in the FVTD algorithm. Since the ingoing 'fluxes' in the source plane are known, this inherently constitutes an RBC. For broadband characterization of a device a modulated Gaussian pulse is used as excitation.

2.4. Scattering parameters

To perform a full-wave S-parameters extraction, a port plane (similar to a source plane) is embedded in the mesh. On each of the discretized triangles of this plane the separated incoming and outgoing 'fluxes' (pre-calculated in the frame of the FVTD algorithm) are used to determine the tangential E - and H -fields belonging to the incident and the reflected waves in the feed line [7], see Equation (4). Using these fields the frequency-domain S-parameters are computed performing a discrete Fourier transform (DFT).

2.5. Near-field to far-field transformation (NFFF)

To compute the far-field radiation pattern, Love's equivalent principle is used [8]. The radiation integrals are solved on an imaginary Huygens' surface enclosing the radiating device. On each of the surface's discretized element, the equivalent sources are computed using the tangential fields on the elements. The tangential fields are either obtained using MUSCL or are interpolated from the fields in the surrounding barycentres, depending whether the NFFF box is coincident

with a surface in the mesh or not. The box may have an arbitrary shape, that can be adapted to the problem. For radiating devices located in a spherical computational domain, a spherical NFFF surface is advantageous. The 3D far-field data are extracted first performing a DFT on the equivalent sources and then numerically evaluating the radiation integrals.

2.6. Computational costs

Since the FVTD scheme is applied in an unstructured mesh more geometrical data have to be stored than in the classical FDTD scheme. Additionally, for second-order accuracy in time and space the field components at three different time steps as well as the field gradients have to be stored. This results in an approximately ten times larger memory needed per cell in comparison to FDTD. However, in spite of the larger cost per FVTD cell a significant saving of resources in comparison to classical FDTD can be achieved for complex structures: A drastic reduction of the number of cells is obtained in the inhomogeneous FVTD meshes because of two reasons. First, coarser meshes are sufficient to approximate the structure with the same accuracy. In Reference [9] it is stated that conformal meshing of a cylinder allows four times larger cell sizes compared to a staircased mesh if the same accuracy should be obtained. In three spatial dimensions this gives a 64 times smaller number of conformal cells needed in the mesh. Second, huge volume ratios of large cells to small cells in the mesh are possible. The inhomogeneous mesh of the broadband double-ridged horn antenna contains roughly 3 millions tetrahedrons. The smallest cells exist in the coaxial cable, where the mesh can be locally assumed as uniform. To fill the whole model with this uniform mesh, approximately 200 millions cells are needed. This results in a ratio of uniform to conformal cells of 67, giving a memory saving factor of about 6.7. Additionally local time steps can be applied in an inhomogeneous mesh [10]. In the presented case the fundamental time step Δt is applied in the feeding region, whereas at the outer computational boundary a time step of $4\Delta t$ can be used.

In the following section, the geometry and the FVTD discretization of the simulation model for the broadband double-ridged horn antenna are discussed.

3. HORN GEOMETRY

Horn antennas are widely used since they have a simple construction, are easy to excite and exhibit large gain. They are employed e.g. as feed elements in satellite tracking systems or communication dishes and they serve as a standard antenna for calibration and gain measurements. Since they exhibit limited bandwidth, great efforts have been made to enlarge the operational bandwidth. Ridges on the side flares are introduced to extend the bandwidth, similar to ridges in a waveguide that expand the separation between the cut-off numbers of its dominant and first higher-order mode. The design of the double-ridged horn antenna reaches back to the late 1950s [3]. Figure 2 shows a 3D view of the simulation model of the double-ridged horn antenna. The geometry of the horn can be decomposed in several parts. There is the feed section (part no. 1 in Figure 2, details are shown in Figure 3) consisting of a coaxial line and a cavity. Two exponentially shaped ridges (no. 2 in Figures 2 and 3) reach from the feed section to the horn aperture and are aligned with the E -plane (y - z -plane). The lower part (with respect to the aperture of the horn) can be seen as a ridged E -plane sectoral horn. The flaps of this part (no. 3) are tilted in the H -plane (x - z -plane). Two wedges (no. 4) are located between them. The

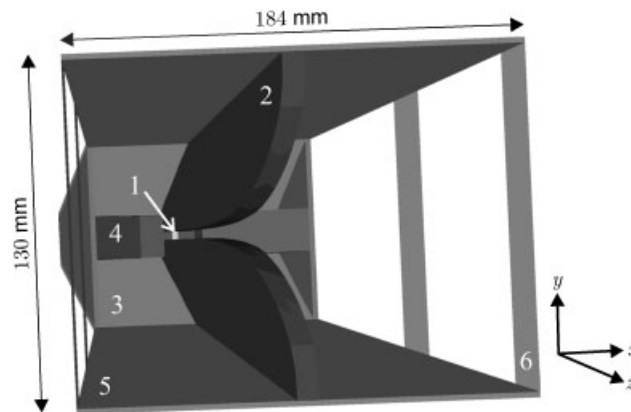


Figure 2. Tilted front view of the antenna model. 1: Feed section, 2: Ridge, 3: Lower flare, 4: Wedge, 5: Upper flare, 6: Copper strap.

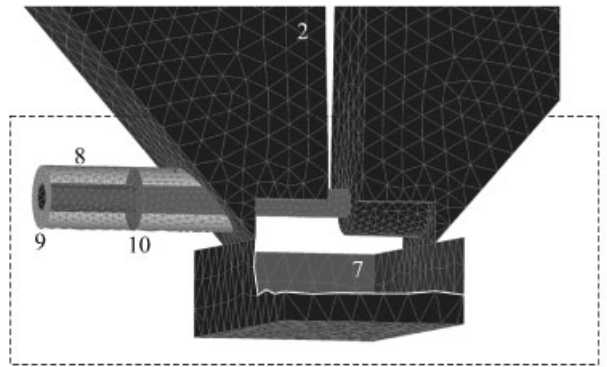


Figure 3. Feeding section of the doubled-ridged horn. 1: Ridges, 2: Cavity, 3: Coaxial feed, 4: Source plane, 5: Port plane. Wedges and other parts are removed for better visualization.

upper part is essentially a pyramidal horn. The upper flaps (no. 5) with a different tilt angle in the H -plane are attached to the lower flares. The flaps tilted in the E -plane are replaced by two copper straps (no. 6) per side which control the width of the radiation pattern for frequencies below 4 GHz [3]. It should be noted, that the wall thickness is included in the model. The dimensions of the aperture are $184 \times 130 \text{ mm}^2$ and the total antenna height is 126.5 mm.

Figure 3 shows the feed section (part no. 1 in Figures 2 and 3) of the double-ridged horn antenna. For better visibility the side flaps are removed and only the ridges (no. 2) with the feeding and the cavity (no. 7, partly cut open) are shown. The input feed consists of a type N input connector followed by a coaxial line (no. 8). This connector is specially manufactured to prevent the excitation of higher-order modes and to support a power level up to 5 kW. The inner conductor of the coaxial line is led through a hole in the first ridge and is connected to the second ridge forming a short circuit. The cavity located below the input section serves as a

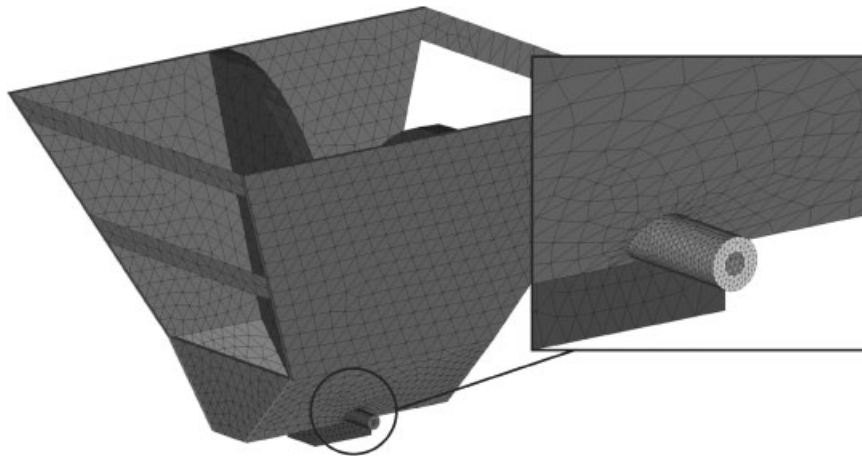


Figure 4. Mesh inhomogeneity in the feed region.

transformer between the coaxial TEM-wave and the ridged-horn field pattern. The transversal source plane (no. 9) and the transverse port plane (no. 10) are embedded in the coaxial cable mesh. Figure 4 shows the surface mesh of the antenna. The strong inhomogeneity of the mesh can be observed in the inset that shows a magnification of the feed section. The transition from the small cells on the coaxial cable to the large cells on the antenna surface is accomplished over a short distance. Thus the total number of cells is reduced significantly. The surface of the coaxial feed is discretized with $\lambda_{\min}/25$, the antenna surface and the outer computational boundary are meshed with $\lambda_{\min}/8$ and $\lambda_{\min}/5$, respectively (wavelengths at 18 GHz). Therewith the volume ratio of the small tetrahedrons in the feed region and the large tetrahedrons in the outer computational area is approximately 1:125. Like in all time-domain techniques, the smallest cell determines the applicable time step for stability, but the 3D explosion of the number of cells is avoided in the inhomogeneous mesh. In Figure 5 the cut-open computational boundary is shown with the double-ridged horn visible in the inside (the volume-filling tetrahedrons are not shown). The upper part of the boundary consists of a hemisphere, whereas the lower section is a truncated cone (frustum). The hemispherical shape is chosen to provide a perpendicular incidence of the radiated waves to the front of the antenna. In the back of the antenna the cone is adapted to the antenna geometry in order to minimize the number of cells. Still the overall computational domain is very large, considering that the hemisphere has a diameter of 17 wavelengths at 18 GHz.

4. RESULTS

The characteristics of the above-described antenna are obtained in the 1–18 GHz frequency range using our FVTD algorithm. The radiation patterns, the return loss and the gain are discussed in the following.

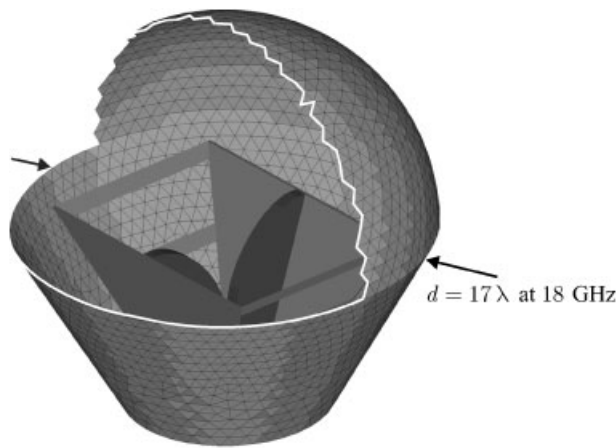


Figure 5. Cut-open computational boundary (with RBC). The horn antenna is visible inside.

4.1. Radiation patterns

Figures 6 and 7 show radiation patterns in the E -plane and H -plane, respectively, of the double-ridged horn antenna obtained by the FVTD simulation. Results at 2, 4, 8 and 16 GHz are displayed normalized to the pattern maximum over all directions. The simulated results are compared to measurements taken from Reference [3] that were performed in an anechoic chamber. The measured radiation patterns are normalized to the simulated ones in broadside direction ($\theta = 0^\circ$). The overall agreement between simulation and measurement is very good over the entire frequency range. All simulation results for all frequencies have been obtained in a single computational run. Although for low frequencies the mesh is very fine ($\sim \lambda_{\max}/140$), the computational boundaries (with RBC) are placed very close to the radiator in terms of wavelengths. That may explain the small difference between the simulation and measurement results at 2 GHz caused by an increased reflection from the RBC. For higher frequencies the mesh of the horn antenna model is coarser ($\sim \lambda_{\min}/8$) but the computational domain is larger (in terms of wavelengths).

From the experimental side, the antenna under test must be irradiated by a plane wave (uniform amplitude and phase). To nearly realize plane wave illumination, the receiving test antenna must be located in the far-field (Fraunhofer) region of the emitting antenna. To fulfil the far-field condition, the two antennas have to be separated by a distance

$$R \geq \frac{2D^2}{\lambda} \quad (7)$$

where D is the largest dimension of the antenna. At a distance R given by (7) the maximum phase deviation in the receiving antenna area between the incident wave and a plane wave is $\pi/8$. In the measurement of the double-ridged horn antenna the plane-wave far-field condition (7) is violated for frequencies larger than $f = 12$ GHz. This problem is believed to be the reason for the discrepancy in Figures 6 and 7 at 16 GHz between the simulation and the measurement.

After successfully validating the simulation results with measurements, full 3D radiation patterns are illustrated in Figure 8 in logarithmic scale for the frequencies 2, 4, 8 and 16 GHz.

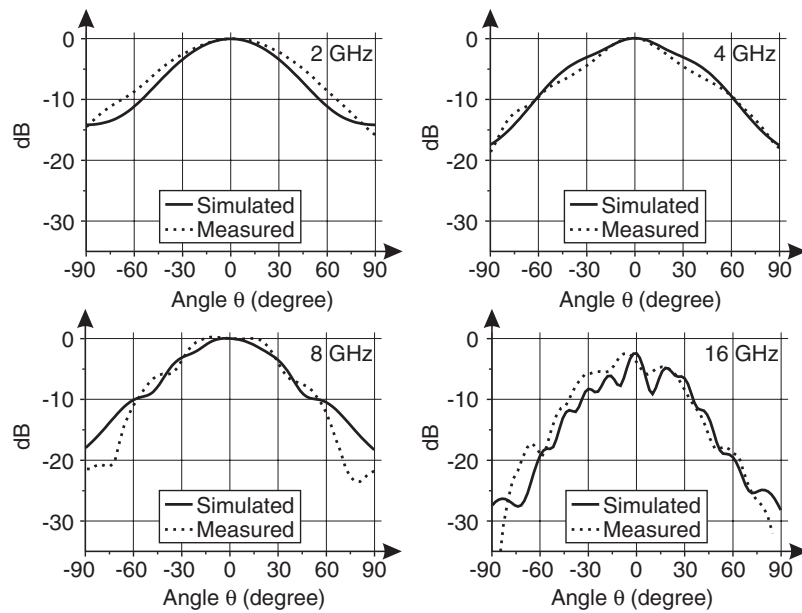


Figure 6. Simulated and measured *E*-plane radiation pattern at 2, 4, 8 and 16 GHz.

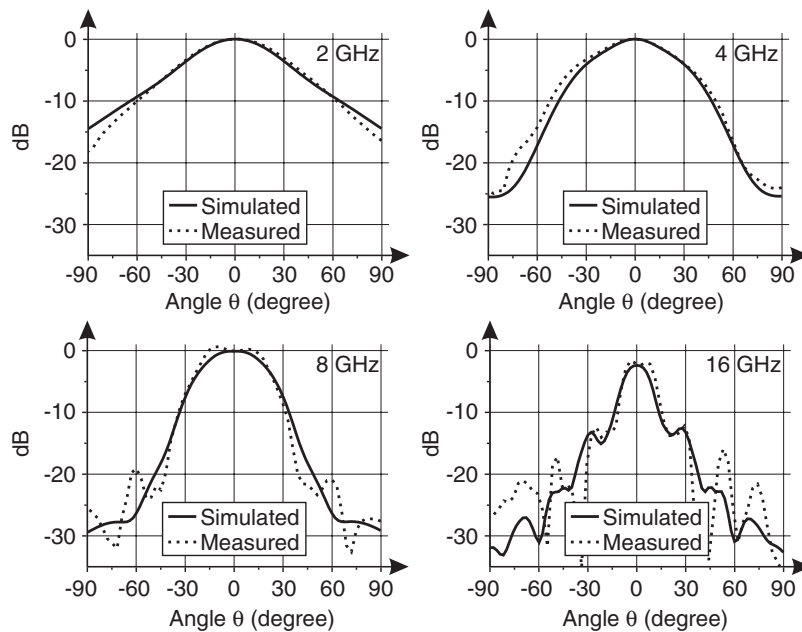


Figure 7. Simulated and measured *H*-plane radiation pattern at 2, 4, 8 and 16 GHz.

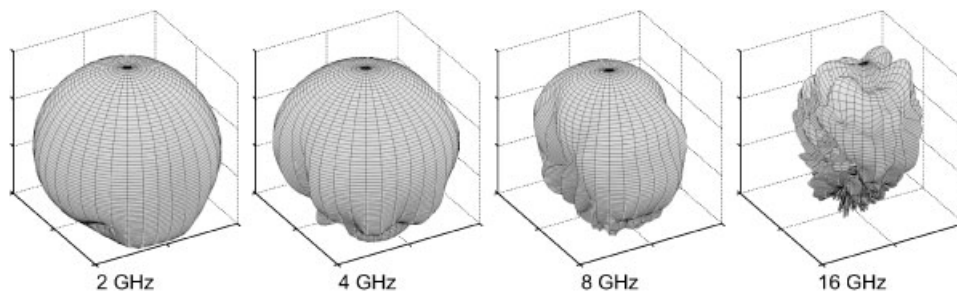


Figure 8. 3D logarithmic radiation pattern from -20 to 0 dB at 2, 4, 8 and 16 GHz.

Considering only the main E - and H -plane radiation patterns, a major drawback of this class of horn antennas at high frequencies remains undetected [3]. At lower frequencies the radiation patterns show, as expected, a good broadside main lobe. For $f > 11$ GHz higher-order modes deform the pattern and four side lobes appear in the diagonal planes of the horn aperture. With increasing frequency, these side lobes become even larger than the broadside lobe.

4.2. Return loss

In Figure 9, the simulated return loss is compared to measured results. The overall agreement is satisfactory, but it should be noted that the double-ridged horn antenna is extremely sensitive with respect to even small geometrical changes. Not every manufacturing detail of the physical horn antenna has been taken into account in the simulation model, e.g. the gaps that exist between the lower and the upper flares.

4.3. Gain

Figure 10 shows the comparison between the simulated broadside gain of the horn antenna and the corresponding measurement. In addition the simulated maximal gain (i.e. over all directions) is displayed. The reflection coefficient S_{11} that is extracted in the simulation is taken into account in the computation of the simulated antenna gain to reproduce the experimental conditions. For discrete frequencies (4, 9, 14, 15, 16 GHz) the 3D radiation patterns in linear scale are shown as well. At 4 GHz the radiation pattern shows the expected well-behaved shape, whereas already at 9 GHz a slight degradation of the pattern can be observed. A strong deformation of the radiation pattern is apparent in the frequency range of $10 \text{ GHz} \leq f \leq 14 \text{ GHz}$ and $f \geq 16 \text{ GHz}$. In this frequency range the broadside and the maximum gain are not coincident, since the main radiation occurs in the 'side' lobes and not anymore in the broadside lobe. At 15 GHz the broadside lobe is showing up again causing the maximum gain to return to the broadside direction. For higher frequencies the broadside lobe disappears again. The discrepancy between broadside simulated and measured gain for frequencies $f \geq 16 \text{ GHz}$ may be caused by the above-mentioned degradation of both measurement and simulation towards high frequencies. Additionally manufacture-caused gaps between the single antenna components (e.g. lower and upper flaps), that are not considered in the model, might play a significant role at high frequencies as investigated in Reference [3].

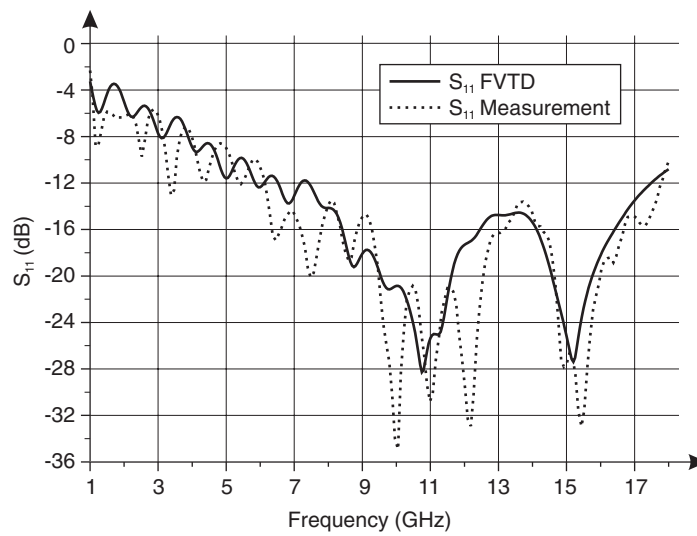


Figure 9. Simulated and measured return loss.

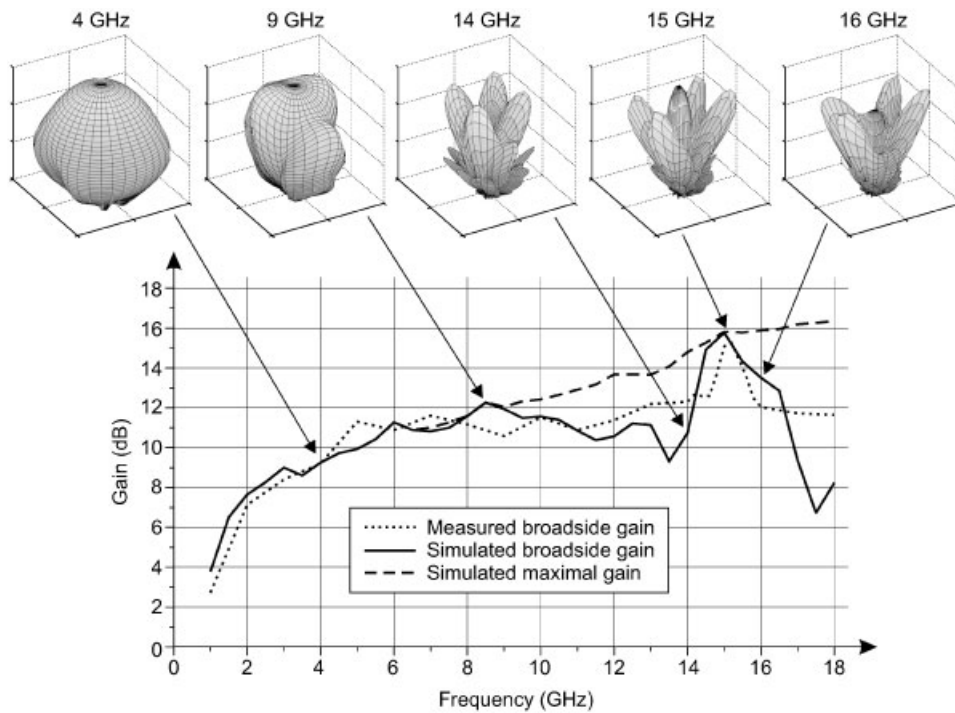


Figure 10. Simulated and measured broadside gain of the double-ridged horn antenna. In comparison the simulated maximal gain is plotted.

5. CONCLUSION

A broadband double-ridged horn antenna was simulated with the FVTD method. The results show the technique's ability to handle complex geometries. Curved and oblique surfaces as well as fine structural details are treated accurately since the core FVTD algorithm works in an unstructured tetrahedral mesh, unaffected by the cells shape and size. In a single simulation run, the near-field data, the radiation patterns and the scattering parameters of the antenna have been calculated for a frequency range of 1–18 GHz. A good agreement was found with the measurement data, showing the accuracy and versatility of the FVTD method applied to practical problems.

ACKNOWLEDGEMENT

The authors acknowledge the help of Christian Bruns and Ralph Brühlmann. This study is supported by the Swiss Defense Procurement Agency (Armasuisse), Bern.

REFERENCES

1. Madsen NK, Ziolkowski RW. A three-dimensional modified finite volume technique for Maxwell's equations. *Electromagnetics* 1990; **10**:147–161.
2. Shankar V, Mohammadian AH, Hall WF. A time-domain, finite-volume treatment for the Maxwell equations. *Electromagnetics* 1990; **10**:127–145.
3. Bruns C, Leuchtmann P, Vahldieck R. Analysis and simulation of a 1–18 GHz broadband double-ridged horn antenna. *IEEE Transactions on Electromagnetic Compatibility* 2003; **45**(1):55–60.
4. Bonnet P, Ferrieres X, Michielsen BL, Klotz P, Roumiguieres JL. Finite-volume time domain method. In *Time Domain Electromagnetics*, Rao SM (ed.), Chapter 9. Academic Press: San Diego, 1999.
5. Altair HyperMesh http://www.altair.com/software/hw_hm.htm [10 December 2003].
6. Yee KS, Chen JS. The finite-difference time-domain (FDTD) and the finite-volume time-domain (FVTD) methods in solving Maxwell's equations. *IEEE Transactions on Antennas Propagation* 1997; **45**(3):354–363.
7. Baumann D, Fumeaux C, Leuchtmann P, Vahldieck R. Finite-volume time-domain (FVTD) method and its application to the analysis of hemispherical dielectric-resonator antennas. *IEEE MTT-S International Microwave Symposium Digest* 2003; **2**:985–988.
8. Balanis CA. *Antenna Theory. Analysis and Design* (2nd edn), Chapter 12. Wiley: New York, 1997.
9. Holland R, Cable VP, Wilson LC. Finite-volume time-domain (FVTD) techniques for EM scattering. *IEEE Transactions on Electromagnetic Compatibility* 1991; **33**(4):281–294.
10. Fumeaux C, Baumann D, Leuchtmann P, Vahldieck R. A generalized local time-step scheme for efficient FVTD simulations in strongly inhomogeneous meshes. *IEEE Transactions on Microwave Theory and Technique*, accepted for publication.

AUTHORS' BIOGRAPHIES



Dirk Baumann received the Dipl. Ing. degree in electrical engineering from the University of Karlsruhe, Germany in 2001. During Spring and Fall 2000, he did an internship at the Alaska SAR Facility (ASF) in Fairbanks, Alaska, working on the calibration of ASF's SAR processor. Currently he is working toward the PhD degree in electrical engineering at the Laboratory for Electromagnetic Fields and Microwave Electronics (IFH), Swiss Federal Institute of Technology (ETH) Zurich, Switzerland. His research interests include numerical methods with emphasis on time-domain techniques and their application to general electromagnetic problems.



Christophe Fumeaux received the diploma and PhD degrees in physics from the Swiss Federal Institute of Technology (ETH) Zurich, Switzerland, in 1992 and 1997, respectively. His PhD thesis on antenna-coupled infrared detectors was awarded the ETH Silver Medal of Excellence. From 1998 to 2000, he was post-doctoral researcher in infrared technology at the School of Optics (CREOL) of the University of Central Florida (UCF), Orlando. In 2000 he joined the Swiss Federal Office of Metrology in Bern, Switzerland, as a scientific staff member. Since 2001, he is a researcher and lecturer at the Laboratory for Electromagnetic Fields and Microwave Electronics (IFH) at ETH Zurich. His current main research interest concerns computational electromagnetics in the time domain for numerical analysis of microwave circuits and antennas.



Pascal Leuchtmann received the diploma on electrical engineering from the Swiss Federal Institute of Technology (ETH) Zurich, Switzerland, in 1980. Afterwards, he was scientific assistant in the electromagnetics group working on theoretical electrical engineering, mainly general purpose numerical calculation of electromagnetic fields. He received his PhD in 1987 from ETH. Currently he is a lecturer for electromagnetics and leads the research groups EMC and antennas at the Laboratory for Electromagnetic Fields and Microwave Electronics (IFH) at ETH Zurich.



Rüdiger Vahldieck received the Dipl. Ing. and the Dr. Ing. degrees in electrical engineering from the University of Bremen, Germany, in 1980 and 1983, respectively. From 1984 to 1986, he was a Postdoctoral Fellow at the University of Ottawa, Canada. In 1986, he joined the Department of Electrical and Computer Engineering at the University of Victoria, British Columbia, Canada, where he became a Full Professor in 1991. During Fall and Spring of 1992–'93 he was a visiting scientist at the 'Ferdinand-Braun-Institut für Höchsfrequenztechnik' in Berlin, Germany. In 1997 he accepted an appointment as Professor for electromagnetic field theory at the Swiss Federal Institute of Technology, Zurich, Switzerland, and became head of the Laboratory for Electromagnetic Fields and Microwave Electronics (IFH) in 2003. His research interests include computational electromagnetics in the general area of EMC and in particular for computer-aided design of microwave, millimetre wave and opto-electronic integrated circuits. Professor Vahldieck is a Fellow of the IEEE. He received the J.K. Mitra Award of the IETE (in 1996) for the best research paper in 1995, and was co-recipient of the outstanding publication award of the Institution of Electronic and Radio Engineers in 1983. Since 1981 he has published more than 230 technical papers in books, journals and conferences, mainly in the field of microwave CAD. He is the Past-President of the IEEE 2000 International Zurich Seminar on Broadband Communications (IZS'2000) and since 2003 President and General Chairman of the International Zurich Symposium on Electromagnetic Compatibility. He is a member of the editorial board of the IEEE Transaction on Microwave Theory and Techniques. From 2000 until 2003, he served as an Associate Editor for the IEEE Microwave and Wireless Components Letters and has now become the Editor-in-Chief effective January 2004. Since 1992 he serves on the Technical Program Committee of the IEEE International Microwave Symposium, the MTT-S Technical Committee on Microwave Field Theory, and in 1999 on the TPC of the European Microwave Conference. From 1998 until 2003, Professor Vahldieck was the chapter chairman of the IEEE Swiss Joint Chapter on MTT, AP and EMC.